Floquet surface hopping: Laser-driven dissociation and ionization dynamics of H_2^+

T. Fiedlschuster,[1,2] J. Handt,[1] and R. Schmidt[1,*]

[1]*Institut für Theoretische Physik, Technische Universität Dresden, D-01062 Dresden, Germany*

[2]*Max-Planck-Institut für Mikrostrukturphysik, Weinberg 2, D-06120 Halle, Germany*

(Received 8 March 2016; published 12 May 2016)

A quantum-classical approach is developed to describe the strong-field molecular dynamics of H_2^+, taking into account all degrees of freedom and simultaneously dissociation as well as ionization. The electron and nuclei are treated correlated, by propagating the nuclei stochastically on potential energy surfaces. It is demonstrated that Floquet surface hopping (FSH) is particularly well suited to describe the laser-driven dynamics. The method is tested against exact solutions of the time-dependent Schrödinger equation, where available. In addition, the FSH results are in excellent agreement with recent experimental data of the dissociation and ionization dynamics of H_2^+. As an additional issue of this work, the primary importance of the focal volume average is worked out for the understanding of experimental results. It determines the gross features of the experimental spectra and provides also a natural explanation of the puzzling saturation effect in the dissociation spectra, observed experimentally. Future applications and further extensions of the method are discussed.

DOI: 10.1103/PhysRevA.93.053409

I. INTRODUCTION

The exact and complete description of the strong-field molecular dynamics requires the solution of the time-dependent Schrödinger equation (TDSE) for electrons and nuclei, taking into account all degrees of freedom (DOF) as well as all fragmentation and ionization channels. As is well known, this is an inaccessible goal for realistic systems due to the exponential scaling of the numerical effort with the number of DOF and/or the complexity of the contributing reaction channels. Only for the smallest molecule, H_2^+, full-dimensional solutions of the TDSE do exist, restricted, however, to laser fields where ionization can be neglected [1–7]. Inclusion of this channel and, in particular, the description of larger systems requires inevitable approximations.

In recent years, surface hopping (SH), in particular Tully's fewest switching algorithm [8], became a very popular method of solving the many-body TDSE, approximately. In any SH approach, the electrons are treated quantum mechanically and the nuclei are propagated by classical trajectories on potential energy surfaces. The coupling between the quantum and classical systems is mediated by stochastically switching ("hopping") between these surfaces. In this way, quantum effects in the nuclear dynamics (respectively, electron-nuclear correlations) are approximately included. Consequently, SH goes clearly beyond the so-called Ehrenfest dynamics, in which the nuclei are treated solely classically and are deterministically propagated on only one, mean, explicitly time-dependent electronic potential energy surface, obtained, however, nonambiguously by the variational principle [9]. In contrast, SH is intuitive, as is the choice of the electronic surfaces, which should preferably be adapted to the problem at hand.

A number of different SH schemes which can take into account a laser field explicitly have been developed [10–23]. Here, the hitherto applied surfaces can be divided into two classes:

(1) *Field-free potentials*, which as a rule represent bare Born-Oppenheimer (BO) surfaces, calculated on different levels of time-independent electronic (*ab initio*) many-body theories [13–15,17,19–23].

(2) *Field-induced potentials*, which include the laser field, and therefore are explicitly time dependent [10–12,16,18].

In the first case, the laser field is taken into account only in the electronic equations of motion (EOM). It induces electronic transitions and nuclear "hops," but will not affect the nuclear motion directly on an actual surface. Consequently, hopping schemes with field-free potentials are well suited to describe realistically the initial electronic excitation process (population of electronic eigenstates) as well as the random choice of the corresponding potentials, at which the nuclear relaxation will start with. Their applications, however, are restricted to laser fields with pulse durations distinctly shorter than the nuclear time scale, typically a few fs [20,22]. Otherwise such approaches can lead to unphysical behavior of the nuclear motion during the laser pulse [12,18].

Laser-driven molecular dynamics can realistically be described only if the laser field is explicitly taken into account in the classical EOM of the nuclei. However, the choice of the field-induced potentials is ambiguous.

One natural way is to diagonalize the instantaneous Hamiltonian including the laser interaction [10,11,16,18]. This yields surfaces arising from so-called "instantaneous BO states" [10], also termed "instantaneous Stark states" [12] or "quasistatic" states [10]. The nuclei are propagated stochastically on this surface, which are called "quasistatic potentials" [11], or simply "laser-induced potentials" [18]. These surfaces oscillate rapidly with the carrier frequency of the laser, which complicates the construction of a clear physical picture of the nuclear dynamics and may lead to serious numerical problems within the hopping [12].

On the other hand, Floquet surfaces have turned out to be extremely useful to illustrate qualitatively different nuclear mechanisms. These, in principle time-independent, surfaces are obtained by diagonalizing the Floquet Hamiltonian [24,25] for a time-periodic laser field. In case of a finite laser pulse, however, they are slowly time dependent via the envelope of the pulse. For diatomic molecules, Floquet surfaces have been widely used from the very beginning of strong-field

*Ruediger.Schmidt@tu-dresden.de

molecular physics to interpret and to understand effects like bond softening [26] and bond hardening [27], multiphoton dissociation [28] and zero-photon dissociation [27,29], dynamical alignment [2,30], and antialignment [31]. Moreover, dynamical calculations on single Floquet surfaces predicted and revealed new effects, like "rotational destabilization" [5] and, very recently, the "elevator effect" [32].

Somewhat surprisingly, up to now, there are only very few attempts to treat the laser-driven molecular dynamics directly on Floquet surfaces, including electron-nuclear correlations via SH [12,18]. Moreover, the hitherto investigations are restricted to one-dimensional model systems, i.e., to diatomic molecules aligned along the laser polarization axis and neglecting ionization [12,18].

In this work, a Floquet surface hopping approach (FSH) is presented which describes the laser-driven dynamics of H_2^+, taking into account all DOF as well as dissociation and ionization, simultaneously. Subsequent nuclear and electronic relaxation after the pulse is included as well. First, the reliability of the method is successfully demonstrated by comparing the results with exact solutions of the TDSE (without ionization). Second, it is shown that the full FSH calculations (including ionization) are in excellent agreement with recent measurements of the dissociation and ionization dynamics of H_2^+ [7].

As an additional but important issue of the paper, it is demonstrated that the focal volume effect determines the gross features of the experimental spectra. In particular, it explains the puzzling saturation in the dissociation spectra, observed experimentally.

The paper is organized as follows: In Sec. II the relevant surfaces (Sec. II A) and the FSH method (Sec. II B) are presented. In Sec. III the FSH method is validated by comparing the results with existing exact solutions of the full-dimensional TDSE for highly differential resolved dissociation probabilities. In Sec. IV elaborate Franck-Condon and focal volume averaged FSH calculations are employed to analyze recent experimental data on kinetic energy release (KER) spectra for dissociation as well as ionization. Summary and outlook are given in Sec. V. Computational details are outlined in Appendix A. In Appendix B the focal volume average procedure is specified.

Atomic units are used unless stated otherwise.

II. THEORY

A. Electronic surfaces and appendant states

Electronic surfaces and their corresponding states play a key role in any mixed quantum-classical approach, in particular and obviously in SH schemes. Different, and in principle arbitrary (approximately) complete sets of states can be used to expand the time-dependent electronic state in order to solve the TDSE by coupled differential equations for the expansion coefficients. In contrast, the surfaces on which the classical nuclei are propagated, and thus the corresponding states, are by no means arbitrary and their choice depends strongly on the particular physical situation or phenomena to be described as realistic as possible.

In this work it is intended to simultaneously treat the electronic excitation and the laser-driven nuclear dynamics, the ionization and following Coulomb explosion, as well as the field-free electronic and nuclear relaxation for the H_2^+ molecule exposed to intense fields. Obviously, different surfaces must be employed to realistically describe the whole scenario.

In this subsection, all surfaces and states which will be implemented to formulate the electronic and nuclear EOM are defined in advance. Also their suitability to describe realistically the coupling between the quantum and classical system via SH during the different stages of the dynamics is discussed. Computational details are given in Appendix A.

1. Born-Oppenheimer surfaces

As fundamentals of molecular physics, BO surfaces E and states $|\varphi\rangle$ are obtained by diagonalizing the electronic part of the field-free molecular Hamiltonian,

$$H_{\mathrm{el}}^0(\vec{R})|\varphi_i(\vec{R})\rangle = E_i(\vec{R})|\varphi_i(\vec{R})\rangle, \tag{1}$$

where H_{el}^0 is given by

$$H_{\mathrm{el}}^0(\vec{R}) = T_e + V_{ee} + V_{en}(\vec{R}), \tag{2}$$

with T_e the electronic kinetic energy operator, V_{ee} the electron-electron, and V_{en} the electron-nuclear interaction, treating the nuclear coordinates $\vec{R}$ as parameters. These, in general multidimensional, surfaces are often used to propagate the nuclei in SH methods, where they are usually calculated "on-the-fly" using different methods and levels of *ab initio* electronic many-body theory [33]. In the case of diatomic molecules they depend only on the internuclear separation R. In the simplest case of H_2^+, the field-free center-of-mass electronic Hamiltonian reads

$$H_{\mathrm{el}}^0 = -\frac{\Delta_{\vec{r}}}{2} - \frac{1}{\left|\vec{r} + \frac{1}{2}\vec{R}\right|} - \frac{1}{\left|\vec{r} - \frac{1}{2}\vec{R}\right|} + \frac{1}{R}, \tag{3}$$

where $\vec{r}$ is the electronic position operator, the classical Coulomb repulsion $1/R$ is included for convenience.

In Fig. 1, the two lowest BO surfaces are shown together with the locations of the one- and three-photon resonances for a $\lambda = 800$ nm laser. Around these distances ($R \approx 3.3$

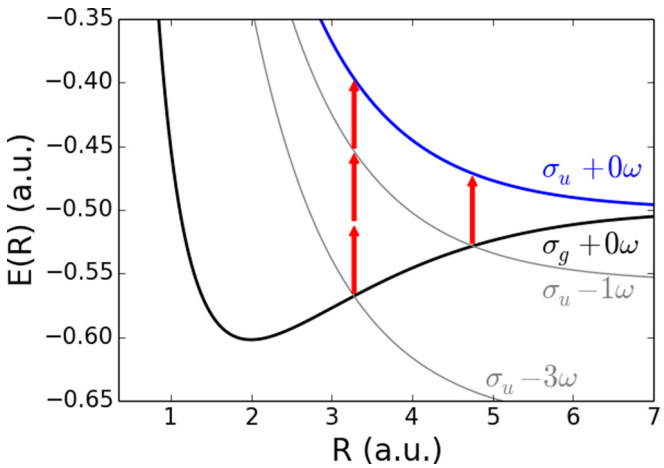

FIG. 1. The two lowest BO surfaces σ_g and σ_u for H_2^+, dressed with different photon numbers for a laser with $\lambda = 800$ nm. The arrows, each with a length of $\hbar\omega$, mark the points of resonant one- and three-photon absorption, which are also easily identified via the crossings between different dressed state surfaces.

and $R \approx 4.7$) electronic transitions will preferentially happen. However, in a hopping scheme between BO surfaces, for the nuclear motion these distances are by no means distinguished from other regions and, thus, hops can be expected to occur at arbitrary distances (see also Sec. II B 3). Moreover, well-established strong-field phenomena of the nuclei, like dynamical alignment [2,30] and antialignment [31] or bond softening [26] and bond hardening [27] can trivially not be described, since BO surfaces do not depend on the molecular orientation and the field strength, respectively. BO surfaces are, however, an extremely useful starting point to construct realistic, field-dependent potentials for the nuclear motion, as will be discussed in the next subsection.

2. *Dressed state and Floquet surfaces*

Floquet surfaces have been widely used to discuss, to interpret, and to visualize many strong-field phenomena in the past (see references in Sec. I and, e.g., [34,35]). Properties of Floquet states and surfaces, as well as dressed states and surfaces, are discussed in the following.

For electrons in a laser field the Floquet Hamiltonian is defined as

$$H_{\mathrm{F}} = H_{\mathrm{el}}^{0} - \vec{\mu} \cdot \vec{F} \cos(\omega s) - i\,\partial_s. \tag{4}$$

The interaction of electrons and laser is included in the length gauge, $\vec{\mu}$ is the dipole operator, and $\vec{F}$ is the amplitude of the electric field of the laser with carrier frequency ω, the time is denoted by s. In this subsection, only cw lasers are considered, where Floquet theory applies exactly. The Floquet Hamiltonian depends parametrically on the nuclear coordinates and the orientation towards the laser polarization direction, in case of a diatomic molecule the bond length R and the alignment angle ϑ, as well as the laser amplitude $\vec{F}$ and the laser frequency ω. Note that the Floquet Hamiltonian acts on an enlarged Hilbert space, the product space of the electronic Hilbert space and the space of all square-integrable $\frac{2\pi}{\omega}$-periodic functions, $\mathcal{H} = \mathcal{H}_{\mathrm{el}} \otimes \mathcal{L}^2_{2\pi/\omega}$. Using the set of functions $\{e^{in\omega s} : n \in \mathbb{Z}\}$ as orthonormal basis in $\mathcal{L}^2_{2\pi/\omega}$, the term $-i\,\partial_s$ is interpreted as an operator describing the amount of energy ($\hbar\omega$ times the number of photons n) exchanged between molecule and laser field. The reader interested in the mathematical details is encouraged to have a look at [25].

The Floquet Hamiltonian in case of vanishing interaction is used to define dressed BO states (short, dressed states) $|\phi\rangle$ and the corresponding energy surfaces:

$$H_{\mathrm{F}}^{0}|\phi_{im}\rangle = \left(H_{\mathrm{el}}^{0} - i\,\partial_s\right)|\phi_{im}\rangle = (E_i + m\omega)|\phi_{im}\rangle, \tag{5}$$

where m is a photon number index. Like the BO states, the dressed states $|\phi\rangle = |\phi(\vec{R})\rangle$ depend parametrically on the nuclear geometry. Using the BO states $|\varphi\rangle$, a coordinate representation of the dressed states is given by

$$\langle \vec{r}, s|\phi_{im}(\vec{R})\rangle = \varphi_i(\vec{r}, \vec{R}) e^{im\omega s}.$$

The dressed state $|\phi_{1,-3}\rangle$, for instance, describes a situation where the electron is in the first excited BO state with three photons absorbed from the field (although not including any interaction). The full set of dressed states $\{|\phi_{im}\rangle\}$ yields an orthonormal basis in $\mathcal{H}$, which, due to its simple relation to BO states, can be used, e.g., to calculate an explicit matrix representation of the Floquet Hamiltonian. Some surfaces appendant to the dressed states are shown in Fig. 1. Besides the energy shift of multiples of $\hbar\omega$, they are identical to BO surfaces, and thus not suited to describe laser-driven molecular dynamics.

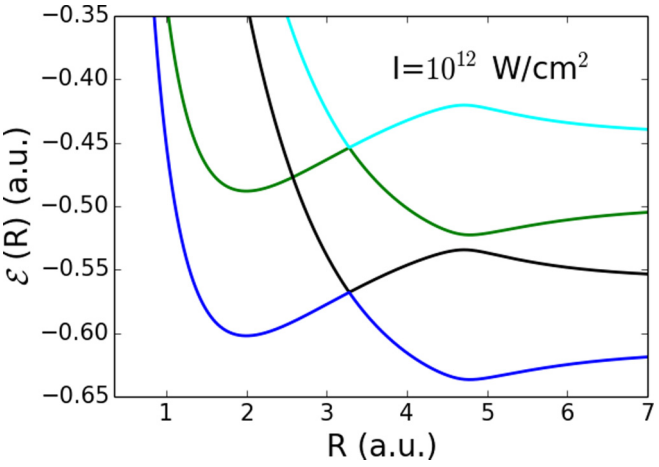

FIG. 2. Four Floquet surfaces for $H_2{}^+$, arising from the two lowest BO surfaces, calculated for $I = 10^{12}$ W/cm^2, $\lambda = 800$ nm, and $\vartheta = 0$. For lucidity only the one- and three-photon crossings are included.

Solving the eigenvalue equation for the Floquet Hamiltonian, *including* the interaction between electron(s) and laser, yields Floquet states $|\Phi\rangle$ and Floquet energies $\mathcal{E}$:

$$H_{\mathrm{F}}|\Phi_a\rangle = \mathcal{E}_a|\Phi_a\rangle. \tag{6}$$

The parametric dependencies of H_{F} are passed to the Floquet states and energies. For a diatomic molecule, in principle, they depend on the four parameters R, ϑ, F, and ω. However, restricting all Floquet-related calculations to the lowest two BO states of $H_2{}^+$, σ_g, and σ_u (which are coupled by the component of $\vec{\mu}$ parallel to the bond axis only), allows for a description using only three parameters $R, F_{\mathrm{eff}} = F\cos\vartheta$, and ω. Fixing the laser frequency, as done in this work, the Floquet surfaces are effectively two-dimensional. Like the dressed states, the full set of Floquet states $\{|\Phi_a\rangle\}$ yields an orthonormal basis in $\mathcal{H}$.

In Fig. 2 a cut along $\vartheta = 0$ for some Floquet surfaces is shown. In wide ranges of R, the Floquet surfaces and the dressed state surfaces coincide. However, there is a remarkable difference: While there are exact crossings between dressed state surfaces at the points of resonant photon absorption, these crossings between Floquet surfaces are avoided. The shape and position of this avoided crossings changes with the (effective) laser intensity I (respectively, I_{eff}) and the laser frequency ω. With increasing intensity, higher order avoided crossings will shift their position towards larger R and will start to open, which leads to an overall less clear physical picture than for lower intensities (for further information see [36]). In Fig. 3, some two-dimensional Floquet surfaces are shown. For intensities below $I \lesssim 10^{13}$ W/cm^2 the angular dependence is relatively weak. Given a high enough intensity, qualitatively new effects, like barriers and trenches in an angular direction, arise. In clear contrast, the BO surfaces, per definition, have no angular dependence at all.

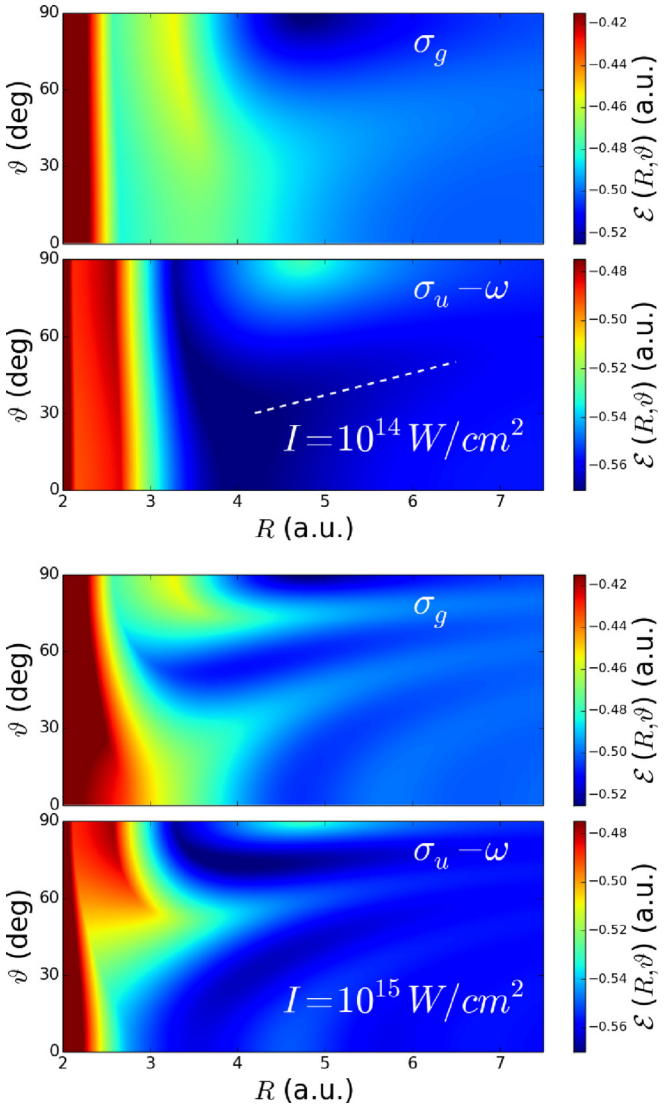

FIG. 3. The Floquet surfaces corresponding to $\sigma_g + 0\omega$ and $\sigma_u - 1\omega$ as a function of R and ϑ for two different laser intensities; the wavelength is $\lambda = 800$ nm. The trench (dashed white line) in the second from top panel is used to explain the angular-resolved dissociation yield in Sec. III. In contrast to Fig. 2, all crossings up to the nine-photon crossing are included, which is necessary for the large intensities used here.

For vanishing intensity $I \to 0$, apart from the avoided crossings, the Floquet surfaces coincide with dressed state surfaces. This is used to label the Floquet surfaces in the following way: If for $I \to 0$ and $R > R_{1\omega}$ for a Floquet surface $\mathcal{E}(R) = E_{\sigma_g/\sigma_u}(R) + m\omega$ holds, the Floquet surface is called "Floquet surface corresponding to $\sigma_g/\sigma_u + m\omega$." Here $R_{1\omega}$ denotes the position of the one-photon resonance.

3. Ionized surfaces

A complete description of the laser-molecule interaction requires the inclusion of ionization. In principle, SH between Floquet surfaces is in particular suited to include this process, which happens preferentially during the laser pulse. In contrast to the mean-field (Ehrenfest) description of ionization [37], SH between Floquet surfaces offers the possibility to decide explicitly between single-, double-, and higher ionization channels by including the corresponding ionized Floquet surfaces. Their correct calculation for many-electron systems, however, is a highly nontrivial task and represents a great challenge for the future. Thereby, approximations will become unavoidable. A reasonable assumption should be to neglect all residual interaction between the ionized electrons and the remaining molecular system. For the one-electron system H_2^+, as considered in this work, this naturally leads to the bare Coulomb surface $V = 1/R$, which determines the nuclear motion after ionization. The coupling between Floquet surfaces and this ionized surface, however, remains a nontrivial problem, even in this simplest case (see Sec. II B 3).

To summarize this part, the SH approach presented in this work is based on the *ad hoc* assumption that the nuclear dynamics proceeds on Floquet surfaces during the pulse. A justification of this assumption can be obtained by comparing the results with exact solutions of the TDSE, where available (i.e., without ionization). Ionization can be approximately taken into account in the present scheme by including the Coulomb surface.

B. Equations of motion

In principle, the Schrödinger equation for the molecule interacting with a laser field has to be solved. Using the dipole approximation, a linear polarized laser, and the length gauge, for H_2^+ in the center-of-mass frame this equation reads

$$i\,\partial_t|\Psi(t)\rangle = \left[T_N + H_{\mathrm{el}}^0 - \vec{\mu}\cdot\vec{F}(t)\cos\omega t\right]|\Psi(t)\rangle, \qquad (7)$$

with H_{el}^0 as introduced in (3), T_N the (relative) nuclear kinetic energy operator, and $\vec{\mu} = q\vec{r}$.

A common starting point for the derivation of practical solvable equations of motion is an expansion of the molecular state $|\Psi(t)\rangle$ into a suitable basis, e.g., the basis of field-dressed BO states $|\phi_{im}\rangle$ introduced in Sec. II A. This expansion reads

$$|\Psi(t)\rangle = \sum_{j=0}^{\infty}\sum_{n=-\infty}^{\infty}\chi_{jn}(\vec{R},t)|\phi_{jn}(R)\rangle, \qquad (8)$$

where the expansion coefficient $\chi_{jn}(\vec{R},t)$ is identified with the position representation of the nuclear state corresponding to the dressed state $|\phi_{jn}\rangle$. Inserting this ansatz in the molecular Schrödinger Eq. (7) yields EOM for the coefficients χ_{jn}. Starting at (8), quantum-classical EOM can be derived in different ways, e.g, by a partial Wigner transformation of the molecular wave function (as done in [12]), or, as done in this work, by assuming localized nuclei ($\chi_{jn}(\vec{R},t) \to c_{jn}(t)\delta(\vec{R} - \vec{R}(t))$, a step which was mathematically rigorously investigated in [38]). The latter approach results in the following.

(1) Hamiltonian equations of motion for the nuclei, which are approximated as purely classical point masses;

(2) a Schrödinger equation for the electronic part of the molecular state;

(3) the need for a self-consistent coupling of electronic and nuclear equations, dealing with the parametric dependencies of the electronic Hamiltonian and establishing a connection between the classical potential surfaces and the electronic state.

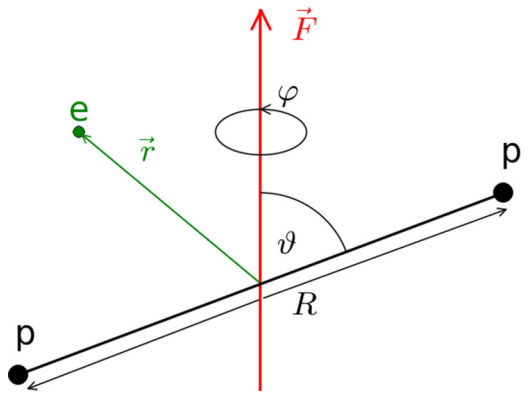

FIG. 4. A sketch of the nuclear degrees of freedom R, ϑ, and φ when considering $H_2{}^+$ in the center-of-mass frame with a fixed direction given by the amplitude $\vec{F}$ of the linear polarized laser field.

The actual way in which 1, 2, and especially 3 are treated defines the FSH method and is presented in the reminder of this section. Computational details are given in Appendix A.

1. Nuclear equations of motion

For the nuclei of a diatomic molecule in the center-of-mass frame, the relevant degrees of freedom are reduced to R,ϑ, and φ, where R denotes the internuclear separation, and the angles ϑ and φ denote the orientation of the internuclear axis to some fixed direction (see Fig. 4). For $H_2{}^+$, a homo-nuclear molecule, the relative nuclear coordinates do not couple to the laser field.

With the reduced nuclear mass M and potential surfaces V_a, the classical Hamiltonian in spherical coordinates reads

$$H = \frac{P_R^2}{2M} + \frac{P_\vartheta^2}{2MR^2} + \frac{P_\varphi^2}{2MR^2 sin^2\vartheta} + V_a(R,\vartheta,\varphi,b),$$

where an index a and a parameter set b (which may be empty) are introduced for later purposes. With the canonical momenta,

$$P_R = M\dot{R}; \qquad P_\vartheta = MR^2\dot{\vartheta} \quad \text{and} \quad P_\varphi = MR^2\sin^2\vartheta\dot{\varphi},$$

Hamilton's equations of motion are

$$\begin{aligned}
\dot{R} &= \frac{P_R}{M}; \quad \dot{P}_R = -\partial_R V_a + \frac{P_\vartheta^2}{MR^3} + \frac{P_\varphi^2}{MR^3\sin^2\vartheta}, \\
\dot{\vartheta} &= \frac{P_\vartheta}{MR^2}; \quad \dot{P}_\vartheta = -\partial_\vartheta V_a + \frac{P_\varphi^2\cos\vartheta}{MR^2\sin^3\vartheta}, \\
\dot{\varphi} &= \frac{P_\varphi}{MR^2\sin^2\vartheta}; \quad \dot{P}_\varphi = -\partial_\varphi V_a.
\end{aligned} \tag{9}$$

Defining ϑ as the angle between $\vec{\mu}$ and $\vec{F}$, φ becomes cyclic and P_φ becomes constant, since none of the surfaces employed in this work depends on φ. It remains to choose the energy surfaces V_a adapted to the physical situation. The following surfaces are used:

(1) Floquet surfaces during the laser pulse,

$$V_a(R,\vartheta,\varphi,b) = \mathcal{E}_a(R,\vartheta,F,\omega).$$

(2) Born-Oppenheimer surfaces when no laser is present,

$$V_a(R,\vartheta,\varphi,b) = E_a(R).$$

(3) The Coulomb surface after ionization,

$$V_a(R,\vartheta,\varphi,b) = 1/R.$$

The surface index a is determined by a surface hopping scheme, which is discussed in Sec. II B 3.

2. Electronic equations of motion

The surface for the propagation of the classical nuclei (see last section) is determined by the time-dependent electronic state $|\psi(\vec{R},t)\rangle$ via a surface hopping scheme (see next section). For this purpose, $|\psi(\vec{R},t)\rangle$ is expanded into dressed states $|\phi_{im}(R)\rangle$. To deal with additional time dependencies, not governed by the Floquet theorem, the (t,t') [in our case (t,s)] method [39,40] is used. While Floquet theory is exact for strictly time-periodic systems, Floquet-based approaches where shown to give reliable results even for short laser pulses including only a few optical cycles [12,41].

The expansion into dressed states reads

$$\begin{aligned}
|\psi(\vec{R},s,t)\rangle &= \sum_{j=0}^{\infty}\sum_{n=-\infty}^{\infty} c_{jn}(t)|\phi_{jn}(R)\rangle \\
&= \sum_{j=0}^{\infty}\sum_{n=-\infty}^{\infty} c_{jn}(t)|\varphi_j(R)\rangle e^{in\omega s}.
\end{aligned} \tag{10}$$

The dressed states $|\phi_{jn}\rangle$ are chosen over the Floquet states $|\Phi_a\rangle$ because of their simpler parametric dependencies. Note that $|\psi\rangle$ is a state in $\mathcal{H} = \mathcal{H}_{\rm el} \otimes \mathcal{L}^2_{2\pi/\omega}$, as briefly discussed in Sec. II A 2. The expansion (10) corresponds to (8) with the further restriction of localized nuclei $\chi_{jn}(\vec{R},t) = c_{jn}(t)\delta(\vec{R} - \vec{R}(t))$. Thus, $|\psi(\vec{R},t)\rangle$ is the solution of the electronic Schrödinger equation along the classical path $\vec{R}(t)$:

$$\begin{aligned}
i\partial_t\psi(\vec{R}(t),\vec{r},t) &= i(\partial_t + \partial_s)\psi(\vec{R}(t),\vec{r},s,t)|_{s=t} \\
&= H_{\rm el}(\vec{R}(t),\vec{r},s,t)\psi(\vec{R}(t),\vec{r},s,t)|_{s=t} \\
&= \left(T_e - \frac{1}{|\vec{r} + \frac{1}{2}\vec{R}(t)|} - \frac{1}{|\vec{r} - \frac{1}{2}\vec{R}(t)|}\right. \\
&\quad \left. - [\vec{\mu}\cdot\vec{F}(t)](\vec{R}(t))\cos\omega s\right) \\
&\quad \times \psi(\vec{R}(t),\vec{r},s,t)|_{s=t}.
\end{aligned} \tag{11}$$

For the ansatz (10), the Schrödinger equation reads

$$\begin{aligned}
i\partial_t|\psi\rangle &= i\partial_t\sum_{j,n} c_{jn}(t)|\phi_{jn}\rangle = H_{\rm F}\sum_{j,n} c_{jn}(t)|\phi_{jn}\rangle \\
&= \left(H^0_{\rm el} - \vec{\mu}\cdot\vec{F}\cos(\omega s) - i\partial_s\right)\sum_{j,n} c_{jn}(t)|\phi_{jn}\rangle.
\end{aligned}$$

Using the eigenvalue equation for the dressed states (5) and the chain rule for the parametric R dependence yields

$$\begin{aligned}
\sum_{j,n}\dot{c}_{jn}|\phi_{jn}\rangle = &- i\sum_{j,n} c_{jn}\left\{E_j + n\omega\right. \\
&\left. - \frac{\vec{\mu}\cdot\vec{F}}{2}(e^{i\omega s} + e^{-i\omega s}) - i\dot{R}\partial_R\right\}|\phi_{jn}\rangle.
\end{aligned}$$

After applying the scalar product with another dressed state $|\phi_{im}\rangle$,

$$\langle\phi_{im}|\cdot|\phi_{jn}\rangle = \frac{\omega}{2\pi}\int_0^{2\pi/\omega} ds e^{-im\omega s}\langle\varphi_i|\cdot|\varphi_j\rangle e^{in\omega s},$$

the final result is

$$\dot{c}_{im} = -ic_{im}(E_i + m\omega) + i\sum_{j,n} c_{jn}\left\{\frac{\vec{\mu}_{ij}\vec{F}}{2}(\delta_{n,m-1}+\delta_{n,m+1}) + i\dot{R}\langle\varphi_i|\partial_R|\varphi_j\rangle\delta_{nm}\right\}. \quad (12)$$

3. Coupling between nuclei and electrons

The impact of the classical motion on the electronic state is accounted for by an alternating propagation of classical and quantum-mechanical EOM, where the nuclear parameters in the electronic EOM are updated with appropriate time steps.

The time-dependent electronic state determines the force in the classical EOM via the (index of the) potential surface. As discussed in Sec. II A, the choice of the surfaces has to be adapted to the physical situation. During the pulse, hopping between Floquet surfaces by an adaption of Tully's fewest switching algorithm [8] is used. The hopping probability to the Coulomb surface is based on the time-dependent ionization probability. Tully's fewest switching algorithm with BO surfaces is used when no laser is present.

Hopping between Floquet surfaces. For the hopping between Floquet surfaces $\mathcal{E}$, the electronic state is expanded into Floquet states $|\Phi_a\rangle$:

$$|\psi(\vec{R},t)\rangle = \sum_a d_a(t)|\Phi_a(\vec{P})\rangle, \quad (13)$$

where $\vec{P} = (P_1, P_2, ...)$ stands for multiple parameters, e.g., R, F, ϑ, and ω, which may be time dependent. With the abbreviation $\langle\Phi_a|\partial_P|\Phi_b\rangle = (\partial_P)_{ab}$, the time derivative of the expansion coefficients reads

$$\dot{d}_a = -id_a\mathcal{E}_a - \sum_i \dot{P}_i\sum_b d_b(\partial_{P_i})_{ab}.$$

The probability to find the electron in a certain Floquet state $|\Phi_a\rangle$ changes by

$$\partial_t(d_a^* d_a) = \sum_b\sum_i -2\mathrm{Re}\left(\dot{P}_i d_a^* d_b(\partial_{P_i})_{ab}\right) =: \sum_b\sum_i f_{ab}^i.$$

Assuming the nuclei are currently on the Floquet surface $\mathcal{E}_a$, according to [8] for $a \neq b$ the quantity g_{ab} is defined as

$$g_{ab} := \Delta t\frac{\sum_i f_{ab}^i}{|d_a|^2} = -2\Delta t\mathrm{Re}\left(\frac{d_b}{d_a}\sum_i \dot{P}_i(\partial_{P_i})_{ab}\right), \quad (14)$$

with Δt the time step in the numerical implementation. In case of $g_{ab} < 0$, g_{ab} is set to zero. Then, for $0 \leqslant b \leqslant N, b \neq a$ (with $N < \infty$ the size of the Floquet state basis used in the implementation), $\sum_{j=0}^b g_{aj}$ is compared to an uniform random number $0 < \zeta < 1$. For the first value of b (if there is any) where the sum is larger than ζ, the surface index is switched from a to b. Sometimes g_{ab} is called "hopping probability." It can, however, take numerical values $g_{ab} > 1$, especially at narrow avoided crossings. Comparing $\sum_{j=0}^b g_{aj}$ to $0 < \zeta < 1$ will thus lead to problems whenever more than one g_{aj} gets large at a time. Fortunately, this does not occur in this work. The velocity adjustment in case of a hop is discussed in Appendix A.

Writing all parameters $\vec{P} = (R, \vartheta, F, \omega)$ relevant for the Floquet states explicitly, (14) reads

$$g_{ab} = -2\Delta t\mathrm{Re}\left(\frac{d_b}{d_a}(\dot{R}\langle\Phi_a|\partial_R|\Phi_b\rangle + \dot{F}\langle\Phi_a|\partial_F|\Phi_b\rangle + \dot{\vartheta}\langle\Phi_a|\partial_\vartheta|\Phi_b\rangle) + \dot{\omega}\langle\Phi_a|\partial_\omega|\Phi_b\rangle)\right). \quad (15)$$

It should be noted that $(\partial_F)_{ab}$, arising from the laser field, is often considerably larger than $(\partial_R)_{ab}$, arising from the molecular structure, such that for short ($\approx$ 25 fs total time) and intense ($I \approx 10^{14}$ W/cm^2) pulses typical values of $\dot{R}(\partial_R)_{ab}$ and $\dot{F}(\partial_F)_{ab}$ are of the same order of magnitude. For the situations considered in this paper $\dot{\vartheta}(\partial_\vartheta)_{ab}$ is rather small compared to the former terms and $\dot{\omega} = 0$ holds.

The coupling $(\partial_R)_{ab}$ for two different laser intensities is shown in the lower panel of Fig. 5 together with the amplitude of the dipole coupling between the two lowest BO states $\langle\sigma_g|\vec{\mu}\cdot\vec{F}|\sigma_u\rangle$. There is a remarkable difference, particularly important for SH. The amplitude of the dipole coupling is nearly a straight line; the physical important regions of resonant photon absorption are not distinct from other regions.

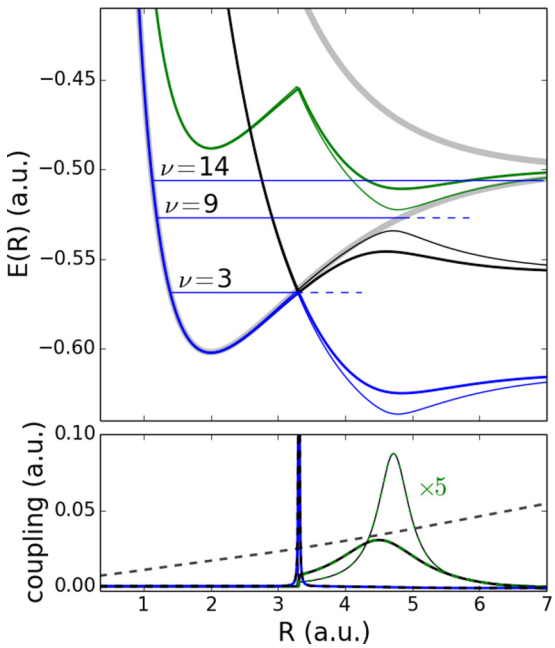

FIG. 5. (Upper panel) The BO surfaces σ_g and σ_u (thick gray lines) and three Floquet surfaces for $\lambda = 800$ nm and $I = 10^{12}$ W/cm^2 (thin colored–black lines) as well as $I = 10^{13}$ W/cm^2 (thick colored–black lines). The vibrational energies for $\nu = 3,9,14$ are indicated for the discussion in Sec. III. (Lower panel) The amplitude of the dipole coupling between σ_g and σ_u for $I = 10^{13}$ W/cm^2 (dashed gray line) and the coupling between the Floquet surfaces as discussed in the text (thin lines for $I = 10^{12}$ W/cm^2 and thick lines for $I = 10^{13}$ W/cm^2; the coupling at the one-photon crossing is scaled by a factor of 5 for both intensities).

This is one reason why hopping between the BO surface in the presence of a laser fails. For the Floquet surfaces, the coupling $\dot{R}\langle\Phi_a|\partial_R|\Phi_b\rangle$ is shown for an arbitrary, yet reasonable, $\dot{R} = 0.01$. In clear contrast to the dipole coupling, it is located at the regions of resonant photon absorption. It is extremely narrow and large for a closed avoided crossing, practically always leading to a nonadiabatic transition (a "hop"). When the avoided crossing opens with increasing laser intensity, the coupling gets smaller and more widespread. This comes with a finite probability for a hop in the vicinity of the points of resonant photon absorption. However, the wider the crossing opens, the more probable the adiabatic passage through the avoided crossing (no hop) becomes. This behavior of the couplings allows for a surface hopping-based propagation which exactly leads to the dissociation pathways often used in the discussion of laser-driven dynamics of H_2^+ (see, e.g., Sec. III or the references in Sec. I).

Hopping to the Coulomb surface. Treating H_2^+ with FSH, ionization is described by hopping to the Coulomb surface $V = 1/R$. The hopping criterion for this is as follows: With $N(t)$ the probability for the electron to be found in any bound state, the probability for ionization during a finite time step Δt is

$$P_i(\Delta t) = N(t - \Delta t) - N(t). \tag{16}$$

This P_i is compared to a uniform random number $0 < \zeta < 1$, and if $\zeta < P_i$ holds, the propagation of the nuclei is continued with the Coulomb surface. In the other case, for $\zeta \geqslant P_i$, the considered trajectory stays bound, thus $N(t)$ is set to 1. Note that, after the evaluation of (16), there are only two valid values for $N(t)$. Either the trajectory is bound ($N(t) = 1$) or it is ionized ($N(t) = 0$). Allowing for $0 \leqslant N(t) \leqslant 1$ leads to serious physical problems, e.g., for long pulses [36]. For practical reasons it is beneficial to allow for $0 \leqslant N(t) \leqslant 1$ and change the hopping criterion (16) to

$$P_i(\Delta t) = \frac{N(t - \Delta t) - N(t)}{N(t - \Delta t)}. \tag{17}$$

The question remains of how $N(t)$ can be modeled during the propagation. One approach is to use a rather large dressed state basis (at least several hundred) including continuum states in the expansion (10), allowing for transitions away from bound states and thus an on-the-fly calculation of $N(t)$. Another possibility is to approximate $N(t)$ using fixed-nuclei ionization rates in a cw laser. Both methods are described and compared in detail in [36]. The approach using (precalculated and pulse-shape independent) ionization rates Γ turns out to give surprisingly good results and is much faster than the approach with the large dressed state basis, therefore it is used in the following. With Γ known, $N(t)$ is modeled as

$$N(t) = e^{-\int_{t_0}^{t} dt'\Gamma(t')} \approx \prod_{i=0}^{n-1} e^{-\Delta t\Gamma(t_0 + i\Delta t)}, \tag{18}$$

where Δt is the numerical time step for the hopping, $n = (t - t_0)/\Delta t$ and $\Gamma(t)$ is the cw-laser ionization rate with the laser intensity matching the pulse envelope at time t. Using (18), the hopping criterion reads

$$P_i(t, \Delta t) = 1 - e^{-\Delta t\Gamma(t)}. \tag{19}$$

Later recombination or re-scattering of the electron is neglected. Some details about the calculation of the rates are given in Appendix A.

Hopping between Born-Oppenheimer surfaces. With no laser present, Tully hopping with BO surfaces is used to determine the surface index for, e.g., the relaxation dynamics. In principle, the hopping criterion reads like (15), where now $\vec{P}$ stands for the nuclear coordinates only. However, since the nonadiabatic coupling $\langle\sigma_g|\partial_R|\sigma_u\rangle$ vanishes exactly for H_2^+, the field-free relaxation dynamics in all cases considered in this paper reduce to a propagation of the nuclei either on the σ_g or σ_u surface.

III. COMPARISON WITH EXACT QUANTUM-MECHANICAL CALCULATIONS

As mentioned in Sec. I, there do exist several full dimensional solutions of the TDSE for H_2^+ exposed to moderate laser fields, where dissociation dominates and ionization can be neglected [1–7]. These results can serve as useful reference calculations to test approximate methods. In this section, we compare the FSH results with the exact solutions of the TDSE given in Ref. [6], rather than present new physical results.

The laser pulse has a total duration of $T = 25$ fs (with $\sin^2$-shaped envelope), a wavelength of $\lambda = 800$ nm, and a central peak intensity of $I = 2 \times 10^{14}$ W/cm^2 in all calculations. The FSH results are obtained by propagating 1000 trajectories for each initial vibrational level, with random initial orientations and initial internuclear distances randomly chosen from classical orbits corresponding to different vibrational levels. For consistency, ionization is switched off in the FSH calculations; further details of the calculations are given in Appendix A. All TDSE results are taken from our previous studies [6]. The comparison is presented systematically, by increasing the differential resolution of the dissociation probabilities.

A. Total dissociation probabilities $P_d(v)$

In Fig. 6, the total dissociation probabilities $P_d(v)$ as a function of the initial vibrational level v are shown. Obviously, the agreement between TDSE and FSH results is nearly perfect. In both calculations the probability increases smoothly up to $v = 9$ and decreases for higher v.

Whereas a physical interpretation of this behavior can hardly be obtained from the exact quantum-mechanical solution, the Floquet picture delivers a transparent explanation in terms of the bond softening [26] and bond hardening [27] mechanisms (see Fig. 5).

For the chosen laser frequency, the vibrational energy of the $v = 9$ state is very close to the crossing between the dressed states σ_g and $\sigma_u - \omega$ (Fig. 1). With increasing laser intensity during the pulse, the avoided crossing between the corresponding Floquet surfaces opens up and lowers the barrier at the one-photon crossing [black (middle) Floquet surface in Fig. 5]. This allows FSH trajectories nearly freely to move to larger R, leading to large dissociation probabilities around $v = 9$ (bond softening). On the other side, for larger v values ($v = 14$ in Fig. 5) the upper Floquet surface forms a potential well [green (upper) Floquet surface in Fig. 5] leading to trapping and a decreasing dissociation probability

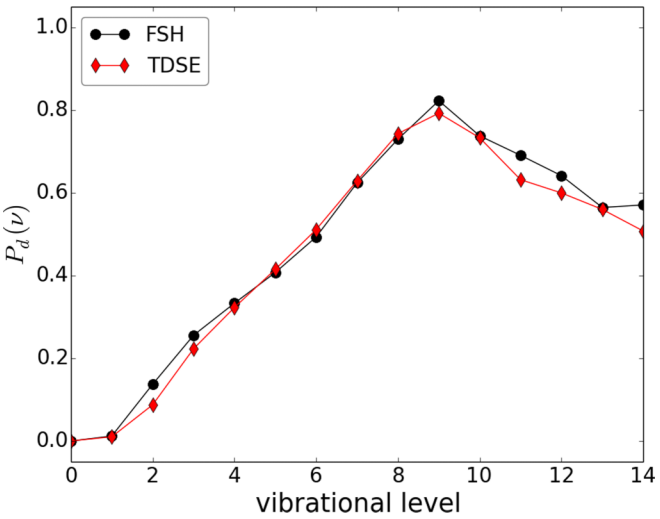

FIG. 6. The total dissociation probabilities $P_d(\nu)$ as a function of the initial vibrational level calculated with the TDSE and the FSH method.

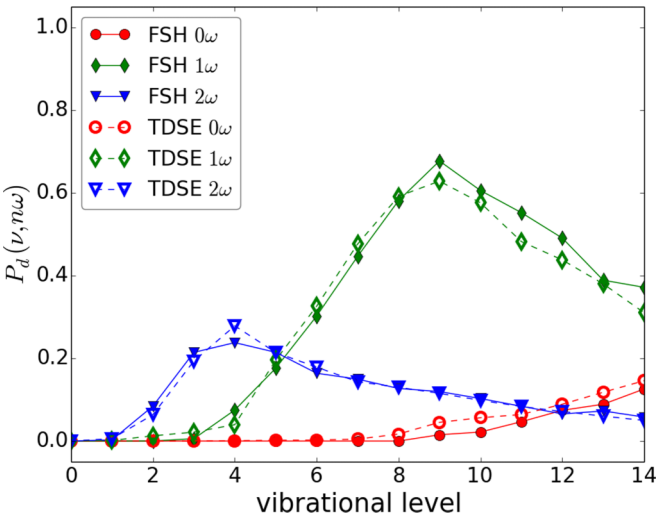

FIG. 7. The photon-resolved dissociation probabilities $P_d(\nu,n\omega)$ with contributions of the zero-, one-, and two-photon channels to the total dissociation probabilities, presented in Fig. 6, calculated with TDSE and FSH.

with increasing ν (bond hardening). Finally, ν values well below $\nu = 9$ (see $\nu = 3$ in Fig. 5) dissociate preferentially via the three-photon resonance (see Fig. 1) on the corresponding Floquet surface [blue (lower) Floquet surface in Fig. 5] and, thus, with distinctly lower probability, as will be shown in the next section.

B. Photon-resolved dissociation probabilities $P_d(\nu,n\omega)$

Both methods, FSH and TDSE, allow one naturally to further analyze and decompose the total dissociation probabilities $P_d(\nu)$ into contributions of individual photon channels $P_d(\nu,n\omega)$. In the TDSE calculations, the photon-resolved dissociation probabilities $P_d(\nu,n\omega)$ are obtained by expanding the nuclear wave function in field-dressed BO states (see [6] for details). In the present FSH calculations, the photon channel is naturally obtained, since for every dissociating trajectory the number of contributing photons is automatically known.

In Fig. 7, the photon-number-resolved dissociation probabilities $P_d(\nu,n\omega)$ contributing to the total probability $P_d(\nu)$ are shown. Again, a very good agreement between FSH and TDSE calculations is observed.

The one-photon dissociation is peaked around $\nu = 9$ due to the bond softening effect discussed above. The two-photon dissociation peaks around $\nu = 4$, which is due to bond softening at the three-photon crossing. An FSH trajectory taking the adiabatic passage at this crossing (no hop) will end up in the two- or three-photon dissociation channel, depending on the subsequent passage (hop or no hop) at the one-photon crossing.

The zero-photon dissociation (ZPD) is most effective for $\nu > 9$, since vibrational trapping is the essential first step for this dissociation mechanism. In the raising edge of the pulse, the deformation of the potential well above the one-photon crossing [see thin and thick green (upper) Floquet surface in Fig. 5] lifts trapped FSH trajectories to higher energies. For some trajectories the energy gain is sufficient to overcome the dissociation barrier, leading to ZPD.

C. Photon- and angle-resolved dissociation probability densities $p_d(\nu,n\omega,\vartheta)$

In Figs. 8–10, the angle- and photon-resolved dissociation probability densities $p_d(\nu,n\omega,\vartheta)$ are shown for $\nu = 4,9,12$. Even for these highly differential quantities a satisfactory agreement between FSH and the TDSE results is found. The dissociation probabilities $P_d(\nu,n\omega)$ and the probability densities shown in this section are related via

$$P_d(\nu,n\omega) = \int_0^{\pi/2} d\vartheta \ \sin\vartheta \ p_d(\nu,n\omega,\vartheta), \tag{20}$$

in case of the TDSE results and via

$$P_d(\nu,n\omega) = \sum_{i=1}^{k} \Delta\vartheta \sin\vartheta \ p_d(\nu,n\omega,i\Delta\vartheta), \tag{21}$$

in case of the binned FSH results.

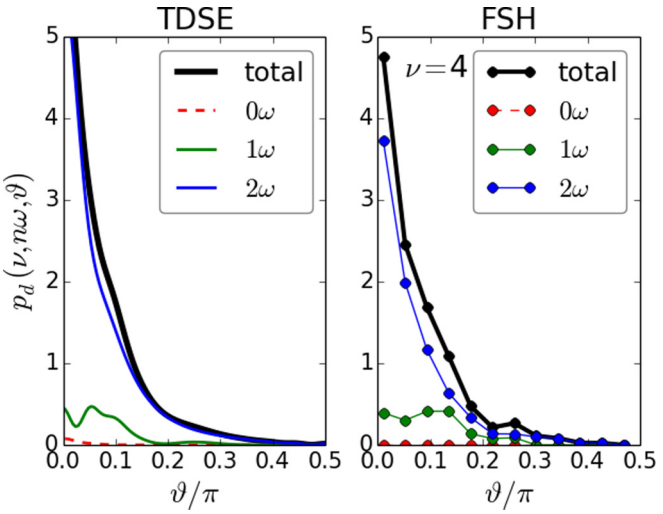

FIG. 8. Photon- and angle-resolved dissociation probability density $p_d(\nu,n\omega,\vartheta)$ for $\nu = 4$, calculated with TDSE and FSH.

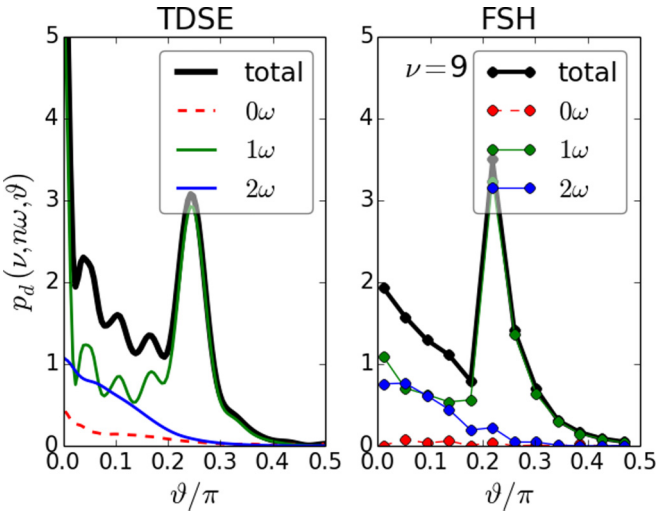

FIG. 9. Photon- and angle-resolved dissociation probability density $p_d(\nu,n\omega,\vartheta)$ for $\nu = 9$, calculated with TDSE and FSH.

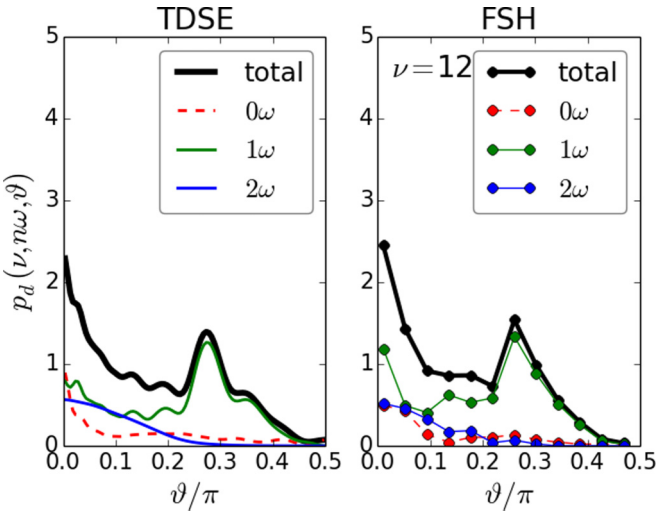

FIG. 10. Photon- and angle-resolved dissociation probability density $p_d(\nu,n\omega,\vartheta)$ for $\nu = 12$, calculated with TDSE and FSH.

For $\nu = 4$ (Fig. 8), the results are dominated by the two-photon channel. A typical path for a trajectory to end up in this dissociation channel is to take the adiabatic passage (no hop) at both the three-photon and one-photon avoided crossing. The adiabatic passage at the three-photon crossing needs a large $I_{\rm eff} = I\cos^2\vartheta$. This leads to an enhanced multiphoton dissociation probability for aligned trajectories, resulting in strongly forward peaked angular distributions.

For $\nu = 9$ (Fig. 9), the one-photon channel dominates the dissociation. With the initial vibrational energy for $\nu = 9$, already a small bond softening effect is sufficient for an adiabatic passage at the one-photon crossing, thus only weak alignment is expected. However, for the chosen laser parameters, the dissociation probability shows a prominent peak at $\vartheta \approx \pi/4$. This peak can be explained with the help of the angular dependence of the Floquet surfaces, as already given intuitively in [6]. It is due to trajectories getting aligned along the trench marked with the dashed line in Fig. 2. For this peak to emerge, quite special laser parameters, tuned to the dissociation dynamics itself, are necessary. An experimental observation of this peak is probably very challenging.

For $\nu = 12$ (Fig. 10), the calculations predict enhanced ZPD for aligned molecules. For small angles ϑ, due to the large effective intensity $I_{\rm eff} = I\cos^2\vartheta$, the potential well above the one-photon crossing lifts considerably within a few fs, leading to a larger probability for ZPD. During the trailing edge of the pulse, however, trajectories contributing to the ZPD channel will be dynamically de-aligned by the laser, resulting in ZPD contributions also at larger angles.

Summarizing this part, a nearly perfect agreement between the approximate FSH and the exact TDSE results for dissociation can be stated. We note in passing that this agreement has been also observed for other pulse lengths ($T = 50$ and $T = 100$ fs) as well as a different intensity ($I = 10^{14}$ W/cm^2) [36]. To what extent the FSH method also applies to describe ionization, can only be proofed by comparing with experimental data, as will be presented in the next section.

IV. ANALYSIS OF EXPERIMENTAL DATA

Recently, the dissociation and ionization dynamics of H_2^+ has been systematically studied in experiments, where the angle-resolved nuclear KER spectra for an 800-nm laser with 7-fs pulse duration are measured within a broad range of intensities (from 2×10^{13} W/cm^2 up to 7.5×10^{15} W/cm^2) [7]. In the first instance, the experimentally observed trends can be summarized as follows.

(i) Weak intensity dependence is observed in the angle-integrated KER spectra for dissociation, showing always a pronounced peak at low energies (centered around 0.8 eV). The spectra exhibit, however, a distinct tail towards larger energies, which is growing up with increasing intensity.

(ii) Strong intensity dependence is observed for the KER-integrated angular distributions for dissociation, which change their functional form, with the general tendency to become narrower with increasing intensity.

(iii) Surprisingly, all these trends are saturated at a certain laser intensity (around $I \approx 10^{15}$ W/cm^2), above which no further changes in the experimental spectra for dissociation have been observed (saturation effect).

(iv) The angle-integrated KER spectra for ionization, however, show an intensity-dependent peak (located at several eV), which continuously moves towards larger energies with increasing intensity. A saturation effect has not been observed.

In [7], the experiments have been beneficially accompanied by theoretical calculations, in which the full-dimensional electronic and nuclear TDSE is solved [3,42]. However, because ionization is not included, the calculations are restricted to low intensities, where dissociation dominates the mechanism. In addition, because the focal volume average is not taken into account, a direct comparison with the experiment is virtually impossible.

In the following, we present a FSH analysis of the data covering the whole range of intensities, including ionization as well as Franck-Condon (FC) and focal volume averaging, allowing also a direct comparison with the experiment.

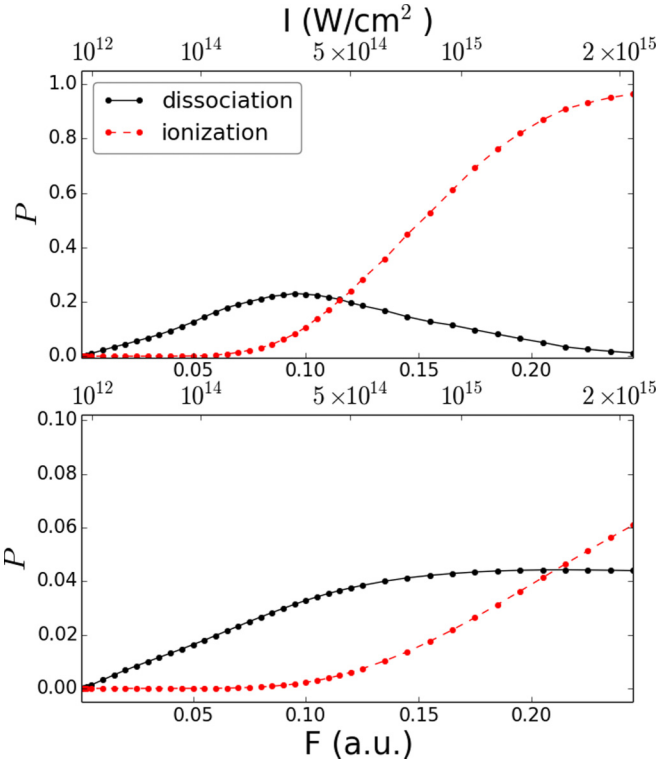

FIG. 11. Total dissociation and ionization probabilities as a function of intensity, calculated without (upper panel) and including (lower panel) the focal volume average.

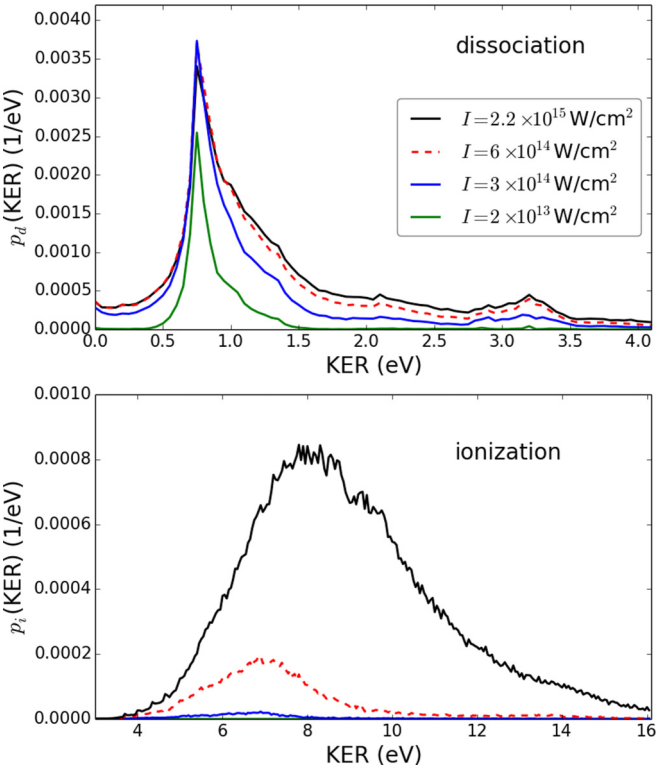

FIG. 12. Angle-integrated probability densities for dissociation (upper panel) and ionization (lower panel) as a function of the KER for different intensities.

Even for the high intensities considered in this section the two-state model (Appendix A) is used. In [7] it was found that for certain initial vibrational levels and KER ranges the contribution of higher states can even dominate the dissociation spectra. These contributions are, however, strongly suppressed in the FC average [7] and even further in the focal volume average.

All results shown in this section (Figs. 11–17) are FC averaged and refer to calculations with the upper given experimental laser parameters, i.e., 800-nm wavelength and 7-fs pulse duration. The factors for the FC average are taken from [43]. For each considered initial vibrational level ($0 \leqslant \nu \leqslant 14$) and each considered peak intensity (see Fig. 11), 3000 FSH trajectories are propagated. Further details of the calculations are given in Appendix A; the focal volume procedure is outlined in Appendix B.

A. Total dissociation and ionization probabilities

For a first orientation, in Fig. 11 the total dissociation (P_d) and ionization probabilities (P_i) as a function of the intensity are shown, calculated without and including the focal volume average. Enormous differences are seen between both calculations. Besides the (more or less expected) differences in the absolute values, the intensity dependence of both quantities P_d and P_i is qualitatively different. Whereas ionization dominates above $I \approx 2 \times 10^{15}$ W/cm^2 and reaches a saturated value of about $P_i \approx 1$ without focal volume average, ionization and dissociation probabilities have nearly equal values at this intensity, if the focal volume effect is included.

Most important, however, the dissociation probability is saturated above an intensity of about $I \approx 10^{15}$ W/cm^2 with a constant $P_d \approx 0.04$, whereas the ionization probability still increases. This is consistent with the experimentally observed saturation in the dissociation spectra, and naturally explains its origin. In this range of intensities, all dissociating molecules feel the same spatial tail of the laser field, and thus the dissociation mechanism becomes independent from the central peak intensity of the laser. This conclusion is indisputably confirmed by looking at more differential quantities, as discussed in the next sections. In the following, the focal volume average is included in all presented theoretical results (Figs. 12–17).

B. Angle-integrated KER spectra

In Fig. 12, the calculated angle-integrated KER spectra (probability densities) are shown for different central peak intensities. The results are in very good agreement with the experimental findings.

The dissociation KER spectra are strongly peaked at an energy of about 0.8 eV, independent on intensity. They exhibit a long-range tail towards larger energies, which becomes more pronounced with increasing intensity. The distributions finally saturate at large intensities, also in accord with experiment. We note that, however, the focal volume-induced saturation effect seems to occur already at somewhat lower intensities in the calculations, as compared to the experiment (see also below). The continuous evolution of the spectra towards higher energies has been qualitatively interpreted in [7] as the consequence

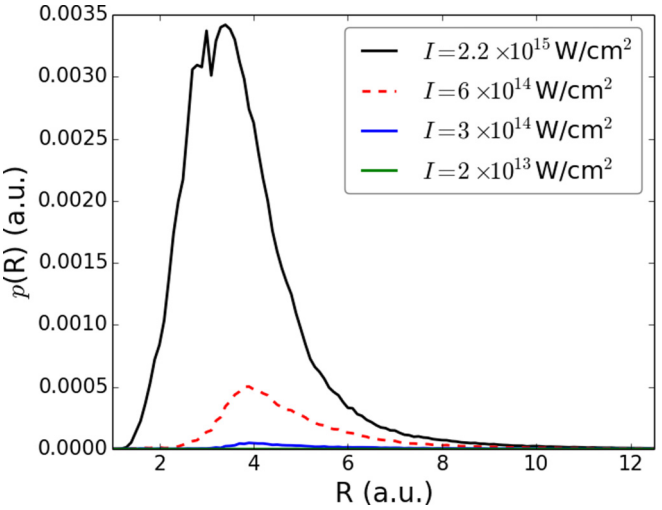

FIG. 13. Ionization probability density $p_i(R)$ as a function of the bond length R (at the time of ionization).

of the increasing role of the 2- and 3-ω dissociation channel. Our photon-resolved calculations confirm this interpretation (see below and [36]). The contribution of the higher-order photon channels are also responsible for the evolution of the KER-integrated angular distributions, as will be shown explicitly in the next section.

The ionization KER spectra in Fig. 12 show a maximum at (naturally) larger energies, with the clear tendency of raising with increasing intensity. This behavior is in accord with the experiment, although the positions of the calculated maxima are slightly shifted towards larger energies as compared to the experimental data (see Fig. 16 in [7]). In [7], the progressive shift towards higher KER with increasing intensity has been qualitatively discussed with the R dependence of the ionization threshold. With increasing intensity, ionization becomes more probable at relatively small internuclear distances (where the ionization threshold is relatively large), leading to higher KER values through the stronger nuclear repulsion. This qualitative interpretation is confirmed by our calculations, where the internuclear distance at ionization is known. As shown in Fig. 13, with increasing intensity the probability for ionization at relative small R grows considerably, naturally leading to a shift towards higher energies in the ionization KER. The low ionization probability for larger R is characteristic for short pulses, where dissociating trajectories reach $R \gtrsim 7$ in the trailing edge or after the pulse, where no ionization will happen. This does not apply to longer pulses, where the ionization KER looks considerably different [36].

C. KER-integrated angular spectra

First and for completeness, we present in Fig. 14 the pure KER-integrated angular distributions for dissociation and ionization as a function of the intensity. In both cases, these distributions become distinctly narrower with increasing intensity. Again, the basic difference between dissociation and ionization consists in the saturation effect for dissociation, which is lacking for ionization.

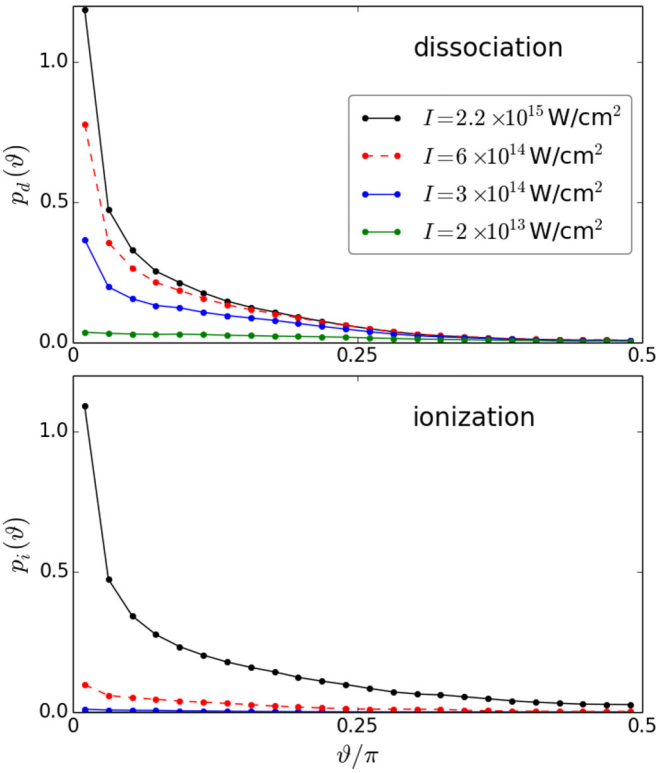

FIG. 14. KER-integrated angular probability densities for dissociation (upper panel) and ionization (lower panel) as a function of the intensity.

Experimentally, the evolution of the angular distributions as a function of the intensity has been analyzed in more detail for dissociation. It was found empirically that the general form of the angular distributions can be fitted by a sum of different $\cos^k \vartheta$ terms, with a single $k = 2$ term for low intensity ($I = 10^{13}$ W/cm^2), $k = 2$ and $k = 10$ contributions for intermediate intensities ($I = 6 \times 10^{14}$ W/cm^2), as well as $k = 2$ and $k = 14$ for the large intensities ($I = 2.5 \times 10^{15}$ W/cm^2), with no further changes above this intensity. Supported by the theoretical calculations, performed at small intensities in [7], it has been argued that this behavior can be possibly understood by the increasing importance of the 3-ω resonance with increasing intensity, together with geometric and dynamical alignment which increases the effective intensity according to $I_{\text{eff}} = I \cos^2 \vartheta$.

In Fig. 15, we present a detailed theoretical, photon-resolved analysis of the angular distributions for dissociation. Evidently, at low intensity the one-photon channel determines the distribution, whereas the two- and three-photon channels become more and more important with increasing intensity. They dominate at the highest intensity and lead to narrow angular distributions. Also shown in Fig. 15, the general form of the calculated distributions can be numerically fitted by exactly the same $\cos^k \vartheta$ terms as found empirically in the experiment, demonstrating impressively a quantitative agreement between theory and experiment.

We note that any direct comparison between theory and experiment must be taken with some caution. In the experiments, events are counted for dissociated or ionized fragments.

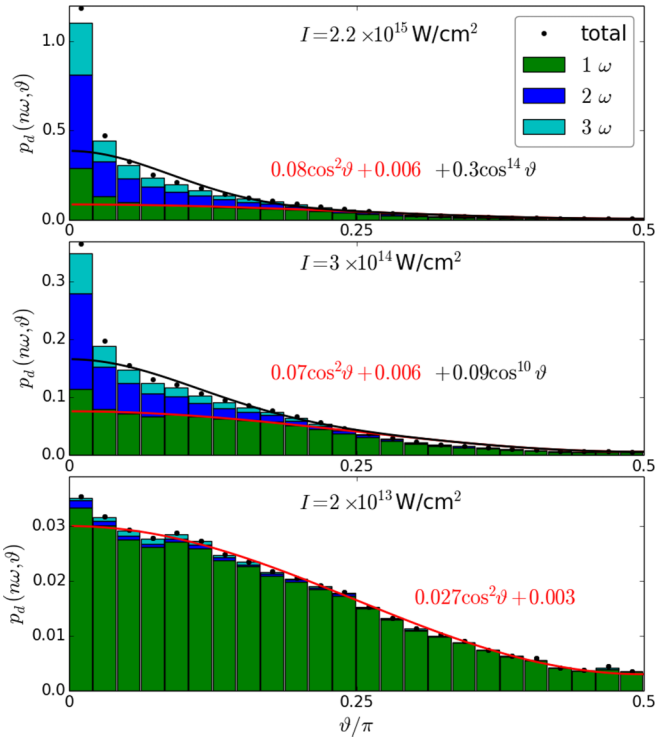

FIG. 15. Photon- ($n=1,2$ and 3) and angle-resolved dissociation probability densities for different intensities. As done in the experimental analysis (Fig. 10 in Ref. [5]), the angular distributions are fitted by individual $\cos^k\vartheta$ contributions with $k=2,10$, and 14, respectively.

Theoretically, normalized probability densities are calculated. In the angular distributions, these densities exhibit a $1/\sin\vartheta$ singularity at $\vartheta=0$, which explains the deviations between the $\cos^k\vartheta$ fits and calculated distributions for the lowest bin at $\vartheta\approx0$ in Fig. 15.

D. Angle-resolved KER spectra

Finally, we compare directly the theoretical and measured angular-resolved KER spectra for dissociation and ionization in Figs. 16 and 17. Obviously, a nice agreement can be stated. We summarize here the remaining differences and discuss future possible improvements of the theoretical analysis.

In the case of dissociation, the theoretical intensities have been chosen slightly lower as compared to the experimental ones, in Fig. 16. This has been done because theoretically the focal volume saturation effect occurs at slightly lower intensities as compared to the experiment (see also above). In experiments, the peak intensity for each laser shot is known only within an uncertainty (of the order of $\pm50\%$). This leads to a distribution of effective peak intensities during the experiment similar to, but independent of, the focal volume effect. The saturation in the dissociation KER will thus shift to slightly larger intensities, where the desired peak intensity is not reached only for a small fraction of the laser shots. In addition, improvements in the fixed-nuclei ionization rates, used for the ionization hopping, are possibly necessary (see below). Furthermore, the calculated spectra show larger multiphoton contributions than the experimental data (see

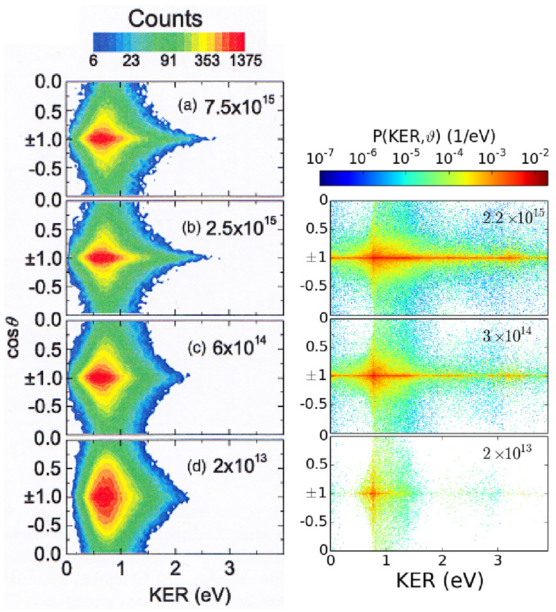

FIG. 16. Experimental (left; adapted from Ref. [7]) and theoretical (right) angle-resolved dissociation KER spectra for different intensities.

Fig. 16 at KER $\approx$ 3 eV). This difference is, at least partially, due to the finite temperature in the experiment (e.g., rotational initial excitation of the molecules) [36].

In the case of ionization, the theoretical calculations overestimate the energetic position of the peak in the spectrum as compared to the experimental value (Fig. 17), as mentioned also above. This clearly indicates that the ionization rates overestimate ionization especially at small internuclear distances, which can be further improved.

Summarizing this part, the following has become apparent.

(1) Disregarding all subtleties, the overall agreement between theory and experiment impressively demonstrates the power of the developed FSH method.

(2) The focal volume average determines the gross features of the experimental trends as a function of the intensity

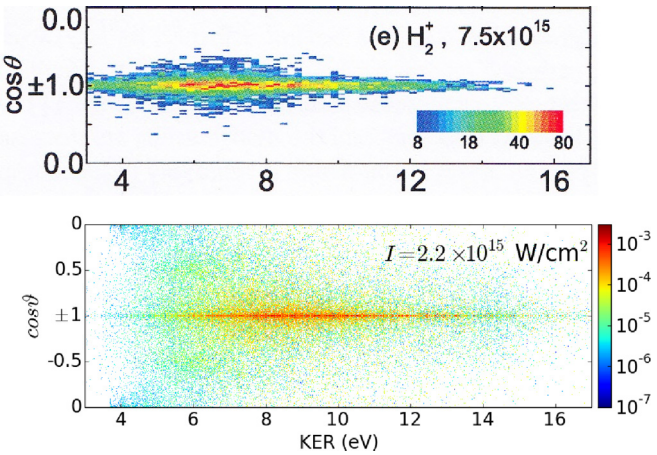

FIG. 17. Experimental (upper panel, number of counts, adapted from Ref. [7]) and theoretical (lower panel, 1/eV) angle-resolved ionization KER spectra.

and, in particular, explains definitely the saturation effect for dissociation.

V. SUMMARY AND OUTLOOK

We have developed a methodology (Floquet surface hopping) to describe the laser-driven dynamics of H_2^+. It takes into account all DOF, simultaneously dissociation and ionization as well as electron-nuclear correlations. The heart of the method consists in a hopping scheme between Floquet surfaces during the laser pulse.

The FSH method is successfully tested against exact solutions of the TDSE at moderate laser intensities (without ionization). In addition, it delivers a quantitative analysis and allows for a detailed interpretation of recent experimental data on dissociation and ionization in strong laser pulses.

As a second issue of the present work, it has become apparent that the focal volume effect determines the gross features of the experimental spectra. In particular, this unavoidable experimental circumstance explains the saturation effect in the dissociation spectra, observed at high intensities.

There remains plenty of room for further extensions and future applications of the method. As an ultimate goal of the theoretical development, the FSH formalism should be extended to include also explicitly the description of the photoelectron spectra. A further desired extension of the existing FSH method consists in its application to many-electron systems. Work in both directions has been started.

Finally we note, despite the successful applications of the FSH approach, demonstrated in this work, it still remains an intuitive method, as any surface hopping approach inherently is. The arbitrary use of Floquet surfaces, instead of others (see introduction), is theoretically by no means founded.

Recently, an alternative quantum-classical approach has been developed, which describes the laser-driven electron-nuclear correlated molecular dynamics without any surface hopping mechanism [44,45]. Here, the nuclei are propagated on a single, so-called "exact" surface. To what extent this method can justify the FSH approach (and/or surface hopping methodology at all) is the subject of ongoing, more fundamental studies [46].

ACKNOWLEDGMENTS

The authors would like to thank M. Fischer for important input at an early stage of the work, and E. K. U. Gross for valuable discussions. We gratefully acknowledge financial support from the Deutsche Forschungsgemeinschaft through the Normalverfahren (Grant No. SCHM 957/10-1).

APPENDIX A: COMPUTATIONAL DETAILS

1. Born-Oppenheimer states and surfaces

To calculate BO states and surfaces, a basis of Gaussian states $|g\rangle$, consisting of 36 states at each nuclear position (same basis as in [6]) is used. BO states $|\phi\rangle = \sum_a c_a|g_a\rangle$ and energies E are obtained by calculating the overlap matrix $S_{ab} = \langle g_a|g_b\rangle$, the matrix representation of the BO Hamiltonian (3) $H_{ab} = \langle g_a|H_{\rm el}^0|g_b\rangle$, and solving the generalized eigenvalue problem,

$$\sum_a c_a(R)\{H_{ba}(R) - E S_{ba}(R)\} = 0, \tag{A1}$$

for $0 < R \leqslant 100$.

2. Floquet states and surfaces

Floquet states and surfaces are obtained by diagonalizing the Floquet Hamiltonian (4) in the basis of dressed states $F_{im,jn} = \langle\phi_{im}|H_{\rm F}|\phi_{jn}\rangle$ (Floquet matrix). Fixing the frequency of the laser field, restricting the BO index in the dressed state basis to $i = 0,1$ and using spherical coordinates with $\vec{F} \parallel \vec{e}_z$ and $\vec{\mu}\cdot\vec{e}_R \equiv \mu_z$, the Floquet matrix is effectively two-dimensional, since

$$\begin{aligned}\vec{\mu}\cdot\vec{F} &= \mu_z F\cos\vartheta + \mu_x F\sin\vartheta\cos\varphi + \mu_y F\sin\vartheta\sin\varphi \\ &= \mu_z F\cos\vartheta\end{aligned} \tag{A2}$$

holds ($\mu_x = \mu_y = 0$ for $i = 0,1$). It is thus sufficient to diagonalize the Floquet matrix as a function of R and F,

$$\begin{aligned}F_{im,jn}(R,F) &= \langle\phi_{im}(R)|H_{\rm F}(R,F)|\phi_{jn}(R)\rangle \\ &= (E_i(R) + m\omega)\delta_{ij}\delta_{mn} \\ &\quad + \frac{\mu_{ij}^z(R)F}{2}(\delta_{m,n+1} + \delta_{m,n-1}),\end{aligned} \tag{A3}$$

which yields Floquet states $|\Phi(R,F)\rangle = \sum_{i,m} c_{im}|\phi_{im}\rangle$ and surfaces $\mathcal{E}(R,F)$. The ϑ dependence is regained by switching from F to $F_{\rm eff} = F\cos\vartheta$. In order to get the coupling matrices for the hopping, $\langle\Phi_a|\partial_R|\Phi_b\rangle$ and $\langle\Phi_a|\partial_F|\Phi_b\rangle$, the derivatives of the Floquet states are calculated by taking the corresponding derivative of the bi-cubic spline representation of the expansion coefficients $c_{im}(R,F)$.

Care has to be taken when choosing the maximal photon number $-m_{\max} \leqslant m \leqslant m_{\max}$. For vanishing interaction ($\vec{\mu}\cdot\vec{F} = 0$), a Floquet state locally coincides with a dressed state ($c_{im}(R) = \delta_{ij(R),mn(R)}$, with j and n changing at each avoided crossing). With increasing interaction ($\vec{\mu}\cdot\vec{F} > 0$), more and more photon numbers m contribute. Choosing $m_{\max}$ too low will eventually lead to errors in the Floquet states and surfaces, noticeable, e.g., in an unphysical behavior of the latter [instead of converging to $E_i + m\omega$ for large R, they bend to higher ($m > 0$) or lower energies ($m < 0$)]. In this work a rather large $m_{\max} = 30$ is used. Together with some additional steps [36], this assures a high quality of the Floquet states (crucial for the hopping) and surfaces (crucial for the nuclear dynamics).

The most demanding task in the calculation of Floquet states and surfaces is to connect the results obtained by diagonalizing the Floquet matrix for fixed parameters R and F in such a way that the result is differentiable with respect to these parameters [36].

3. Fixed-nuclei ionization rates

To model the probability for the ionization hopping, ionization rates $\Gamma(R,\vartheta,F)$ are calculated by solving the fixed-nuclei TDSE for a cw laser in basis expansion. Following [47], the nuclei-centered basis (see Appendix A 1) is augmented

by space-fixed Gaussians, which yields a relatively dense structure of energy levels around $E = 0$ and appendant states.

In principle, localized Gaussian basis functions are not a good choice to represent continuum states ($E > 0$). This prevents us from discussing the dynamics of the ionized electron. To ensure the validity of this method for the calculation of ionization rates, the fixed-nuclei ionization probability in a finite laser pulse is compared to the results of other methods. Very good agreement is found in [36], where also more details of the calculation are given.

4. Trajectory calculations

a. Laser pulses

In Sec. III, a pulse envelope,

$$F(t) = F_{\max} \sin^2\left(\frac{t}{T}\pi\right), \tag{A4}$$

with a total time $T = 25$ fs and $F_{\max} = 0.075$ ($I_{\max} = 2 \times 10^{14}$ W/cm^2) is used. In Sec. IV the pulse envelope reads

$$F(t) = F_{\max} e^{-((t-T/2)/\tau)^2}, \tag{A5}$$

where τ is related to the full width at half maximum (FWHM) of the intensity as $T_{\mathrm{FWHM}} = \sqrt{2\ln 2}\tau = 7$ fs. A total time $T = 2\sqrt{\frac{\ln 100}{2\ln 2}} T_{\mathrm{FWHM}}$ is chosen, such that the intensity at the beginning and the end of the pulse $I(0) = I(T) = 10^{-4} I_{\max}$ is very small compared to the peak intensity.

b. Nuclear EOM

The classical nuclear EOM (9) are solved with the leap-frog algorithm. During the laser pulse, a time step $\Delta t_{\mathrm{cl}} = 0.01$ is used. Ionized trajectories are propagated on the Coulomb surface $V = 1/R$ (during and after the pulse), dissociated trajectories on BO surfaces (during and after the pulse), and all other trajectories are propagated on Floquet surfaces during the pulse and on BO surfaces after the pulse. The forces are calculated by taking the derivative of the cubic (bi-cubic) spline representation of the BO (Floquet) surfaces. The dissociation threshold is taken to be $R_{\mathrm{diss}} = 10$. Trajectories which are not bound at the end of the pulse are propagated until they reach $R = 100$. Here, the time step $0.01 \leqslant \Delta t_{\mathrm{cl}} \leqslant 0.5$ is adapted to the gradient of the potential.

The radial classical initial conditions R_0 and $\dot{R}_0$ are sampled with classical trajectories, propagated in the BO ground-state surface with energies matching the quantum mechanical vibrational energies of H_2^+. This yields different initial conditions for different initial vibrational levels ν. Calculations are done for $0 \leqslant \nu \leqslant 14$. Higher initial vibrational levels are not suspected to give qualitatively new effects; furthermore they have only a small impact on FC-averaged results.

Only rotationally cold initial conditions ($\dot{\vartheta}_0 = 0$, $\dot{\varphi}_0 = 0$) are considered, thus the initial angles ϑ_0 are uniformly distributed between $0 \leqslant \vartheta_0 < \pi/2$. The φ distribution is accounted for by a weight $\sin\vartheta_0$ for each trajectory.

c. Electronic EOM

The set of equations (12) for the expansion coefficients of the electronic state into the dressed state basis is solved using ZVODE [48]. The two-state model ($i = 0,1$) is combined with photon numbers $-20 \leqslant m \leqslant 11$, resulting in 64 basis states. Half of the states, however, can be omitted from the calculation, since states with $i = 0$ and odd m as well as $i = 1$ and even m are not populated during the dynamics. Updating the BO energies and the dipole coupling (which are interpolated from the precalculated data) with a relatively large time step $\Delta t_{\mathrm{qm}} = 5$ is sufficient for convergence of the hopping.

The electronic state at the start of the calculation is the BO ground state dressed with zero photons, $|\phi_{00}\rangle$. The allocation of this initial state to a field-free Floquet state is possible, but depends on R.

d. Hopping

At each classical time step Δt_{cl} during the pulse, all not already ionized trajectories get a chance to hop to the Coulomb surface. The hopping probability is given by (19), which is calculated using fixed-nuclei ionization rates $\Gamma(t) = \Gamma(R(t),\vartheta(t),F(t))$. No velocity adjustment is done in case of a hop to the Coulomb surface. The ionization KER is solely determined by the kinetic energy of the trajectories at the ionization hop and the subsequent relaxation dynamics on the Coulomb surface.

At each classical time step Δt_{cl} during the pulse, all not already dissociated trajectories get a chance to hop to another Floquet surface $\mathcal{E}$ with the hopping procedure described in Sec. II B 3. The hopping probabilities (15) are calculated by transforming the time-dependent electronic state to the Floquet basis. The necessary coupling matrices are calculated prior to the propagation. If a hop (from $\mathcal{E}_a$ to $\mathcal{E}_b$) occurs, the velocity $\vec{v} = \dot{R}\vec{e}_R + R\dot{\vartheta}\vec{e}_\vartheta$ is adjusted along the nonadiabatic coupling vector,

$$\vec{d}_{ab} = \langle\Phi_a|\partial_R|\Phi_b\rangle\vec{e}_R + \langle\Phi_a|\partial_\vartheta|\Phi_b\rangle\vec{e}_\vartheta + \langle\Phi_a|\partial_F|\Phi_b\rangle\vec{e}_F,$$

such that the total energy is conserved. If the velocity adjustment would result in a negative kinetic energy, the hop is rejected. The direction $\vec{e}_F$ is taken parallel to the actual velocity.

During the laser pulse, the field amplitude $0 \leqslant F \leqslant F_{\max}$ changes by orders of magnitude. At the highest $F_{\max} = 0.25$ ($I_{\max} = 2.2 \times 10^{15}$ W/cm^2) considered in the calculations, all avoided crossings between neighboring Floquet surfaces up to the seven-photon crossing start to open considerably. Thus, all crossings up to the nine-photon crossing are included in the Floquet surfaces, states, and coupling matrices. For higher $I_{\max}$, e.g, to match the experimental values used in [7] $I_{\max} = 7.5 \times 10^{15}$ W/cm^2, even higher order crossings ($11\omega, 13\omega, \ldots$) have to be included. All these photon crossings are inevitably present in the calculation also in the leading and trailing edge of the pulse, where most of them are practically closed and the trajectories are supposed to hop with 100% probability. Above hopping procedure can, in principle, deal with this situation. There is, however, a more straight-forward way. In the vicinity of practically closed avoided crossings, a Floquet state $|\Phi\rangle = \sum_{im} c_{im}(R)|\phi_{im}\rangle$ locally coincides with a dressed state $|\phi_{jn}\rangle$, thus $c_{im}(R) \approx \delta_{ij(R),mn(R)}$, with j and n changing exactly at the closed avoided crossing. If such a change occurs a hop is invoked, otherwise the trajectory is subject to the hopping procedure discussed in Sec. II B 3.

APPENDIX B: THE FOCAL VOLUME AVERAGE

The high laser intensities used in modern experiments are achieved by a temporal and spatial focusing of the laser. The spatial focusing leads to a distribution of effective peak intensities $I_{\max}^{\text{eff}}$ "seen" by the molecules in the target area, depending on their distance to the laser focus, where the nominal peak intensity $I_{\max}$ is reached (focal volume effect). In experiments, the obtained data, gathered by measuring many events, is inevitable averaged over these different $I_{\max}^{\text{eff}}$ (focal volume average). Suppressing the focal volume effect directly in the experiment is difficult, since a narrow laser focus is necessary to get high peak intensities. Lowering the target size, if possible at all, comes with lower count rates since the target density has to be kept low enough to prevent interactions between the target ions.

When comparing theoretical calculations to experimental data, the focal volume effect has to be considered either by averaging the results obtained from calculations with different peak intensities (as done in this work), or, the other way around, by an "inverse" focal volume average using experimental data obtained by conducting the same experiment with multiple peak intensities (see, e.g., [49]). To emphasize the importance of the focal volume average, in Fig. 18 the focal volume averaged dissociation KER, discussed in Sec. IV, is compared to the KER calculated for $I_{\max}$ only. The striking differences arise from dissociation contributions at $I_{\max}^{\text{eff}}$, often well below $I_{\max}$. The disagreement ranges from quantitatively (lower panels, where bond softening is dominant for all intensities up to $I_{\max}$) over qualitatively (middle panels, where multiphoton dissociation dominates at $I_{\max}$ but is negligible for most $I_{\max}^{\text{eff}}$), up to the point where the not focal volume averaged result is totally meaningless if compared to experimental data (upper panels, where at $I_{\max}$ the dissociation channel is depleted by ionization).

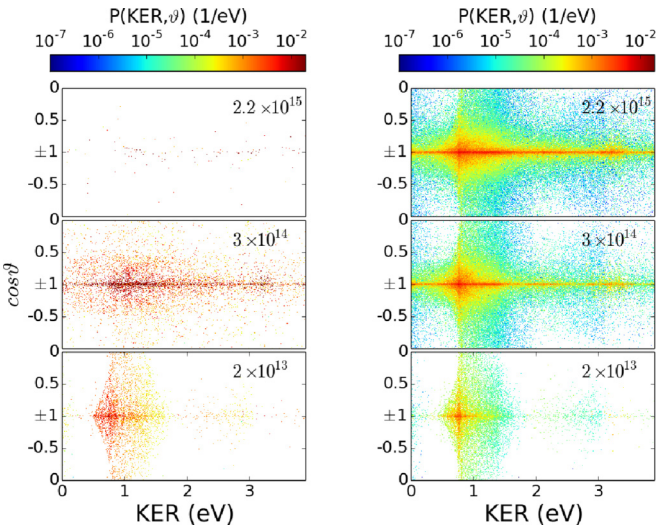

FIG. 18. (Left column) The FC-averaged angular resolved dissociation KER calculated for the peak intensities given in the plots. (Right column) The FC-averaged angular resolved dissociation KER, focal volume averaged to match experimental peak intensities given in the plots (same as Fig. 16).

The main problem when including the focal volume average is the increase of the computational effort, since calculations for different peak intensities are needed. Calculating the weighting factors itself is, with some basic assumptions, a relatively easy task. In the following, it is outlined for an experiment with a collimated ion beam. The situation is simplified by the following considerations.

(1) A homogeneous distribution of the molecules within the beam is assumed; their center-of-mass motion during the pulse is neglected.

(2) For a Gaussian laser beam $\parallel \vec{e}_z$ with peak intensity I_0 and focused to a focal radius w_0, the intensity reads

$$I(\varrho,z) = I_{\max}\left(\frac{w_0}{w(z)}\right)^2 e^{-2(\varrho/w(z))^2}. \tag{B1}$$

The profile along the z axis is determined by $w(z) = w_0\sqrt{1+(\frac{z}{z_0})^2}$, where the Rayleigh length $z_0 = \frac{\pi w_0^2}{\lambda}$ is the point at which the focal radius has broadened to $w(z_0) = \sqrt{2}w_0$. With a typical z_0 much larger than the ion beam width in the z direction, $w(z) \approx w_0$ may be used, hence it is sufficient to consider a two-dimensional intensity profile,

$$I(\varrho,z) \approx I(\varrho) = I_{\max}e^{-2(\varrho/w_0)^2}. \tag{B2}$$

There are two qualitatively different situations, determined by the ratio of the ion beam width b and the diameter of the iso-intensity circle of the onset intensity for, e.g., dissociation. These situations are illustrated in the inset of Fig. 19, where a broad ($b = 8w_0$) and a narrow ($b = 2w_0$) ion beam is shown together with the intensity profile of the laser. A peak intensity of $I_{\max} = 2.2 \times 10^{15}$ W/cm^2 and a cutoff intensity of $I_{\min} = 8.75 \times 10^9$ W/cm^2 is used as for the calculations in Sec. IV. The green circles are iso-intensity lines with equal spacing ΔI [which is also the intensity spacing between the cutoff intensity (black line) and the first green line]. It becomes immediately clear that the majority of ions are subjected to intensities $I_{\max}^{\text{eff}}$

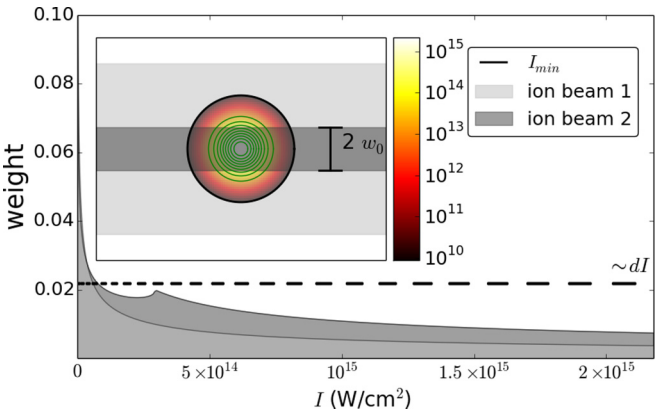

FIG. 19. The focal volume average weights (calculated for a narrow and a wide ion beam; see inset), given in units of the maximal involved weight (belonging to the lowest intensity bin of beam 1). Equidistant bins $dF = 0.001$ are used for the calculation; the bins dI are illustrated by the dashed black line. For both ion beams, the gray area under the curves is normed to 1 (sic). The inset shows the intensity profile (B2) of the laser; some iso-intensity lines (green) are drawn in the pulse area.

much lower than $I_{\max}$ in such a situation. As discussed above, quantities of interest P are automatically averaged according to

$$P = \int_A dA\, P(A).$$

If the width of the ion beam is large enough, such that the surfaces dA of all relevant iso-intensity shells are circular rings, a simple substitution using (B2) yields

$$dA \sim \frac{dI}{I} \sim \frac{dF}{F}.$$

In order to employ the focal volume average, the pulse area is divided into circular rings corresponding to the peak intensities of single calculations $I_{\max}^{\text{eff}} \in [I_{\min}, I_{\max})$ by solving (B2) for ϱ. The weight for a single calculation is given by the normalized overlap of the corresponding circular ring and the ion beam surface. For a wide ion beam (ion beam 1 in Fig. 19) the whole ring surface has to be taken, which leads to focal volume average weights $\sim 1/I$. The same holds for a narrow beam at high intensities (ion beam 2 in Fig. 19), where for low intensities two segment surfaces have to be subtracted.

The resulting weights are shown in Fig. 19 in multiples of the largest involved weight. Since for the width of the narrow beam $b = 2w_0$ is chosen, there is a cusp in the weights located at $I = I_{\max} e^{-2} \approx 0.3 \times 10^{15}$ W/cm^2, the simple $1/I$ dependence only holds for larger I. The quantitative difference in the weights for both ion beams stems from the increasing differences at low intensities. Due to the normalization, this affects the ratio of the weights even when the behavior $\sim 1/I$ holds for both ion beams. For the focal volume average applied in Sec. IV a wide ion beam is assumed.

[1] E. E. Aubanel, J.-M. Gauthier, and A. D. Bandrauk, Phys. Rev. A **48**, 2145 (1993).
[2] E. Charron, A. Giusti-Suzor, and F. H. Mies, Phys. Rev. A **49**, R641 (1994).
[3] F. Anis and B. D. Esry, Phys. Rev. A **77**, 033416 (2008).
[4] M. Winter, R. Schmidt, and U. Thumm, Phys. Rev. A **80**, 031401 (2009).
[5] M. Fischer, U. Lorenz, B. Schmidt, and R. Schmidt, Phys. Rev. A **84**, 033422 (2011).
[6] M. Fischer, F. Grossmann, R. Schmidt, J. Handt, S. M. Krause, and J.-M. Rost, New J. Phys. **13**, 053019 (2011).
[7] J. McKenna, F. Anis, A. M. Sayler, B. Gaire, N. G. Johnson, E. Parke, K. D. Carnes, B. D. Esry, and I. Ben-Itzhak, Phys. Rev. A **85**, 023405 (2012).
[8] J. C. Tully, J. Chem. Phys. **93**, 1061 (1990).
[9] T. Kunert and R. Schmidt, Eur. Phys J. D **25**, 15 (2003).
[10] M. Thachuk, M. Y. Ivanov, and D. M. Wardlaw, J. Chem. Phys. **105**, 4094 (1996).
[11] P. Dietrich, M. Y. Ivanov, F. A. Ilkov, and P. B. Corkum, Phys. Rev. Lett. **77**, 4150 (1996).
[12] I. Horenko, B. Schmidt, and C. Schütte, J. Chem. Phys. **115**, 5733 (2001).
[13] G. A. Jones, A. Acocella, and F. Zerbetto, J. Phys. Chem. A **112**, 9650 (2008).
[14] R. Mitrić, J. Petersen, and V. Bonacic-Koutecký, Phys. Rev. A **79**, 053416 (2009).
[15] I. Tavernelli, B. F. E. Curchod, and U. Rothlisberger, Phys. Rev. A **81**, 052508 (2010).
[16] F. Kelkensberg, G. Sansone, M. Y. Ivanov, and M. Vrakking, Phys. Chem. Chem. Phys. **13**, 8647 (2011).
[17] R. Mitrić, J. Petersen, M. Wohlgemuth, U. Werner, V. Bonacic-Koutecký, L. Wöste, and J. Jortner, J. Phys. Chem. A **115**, 3755 (2011).
[18] J. J. Bajo, J. González-Vázquez, I. R. Sola, J. Santamaria, M. Richter, P. Marquetand, and L. González, J. Phys. Chem. A **116**, 2800 (2012).
[19] J. Petersen and R. Mitric, Phys. Chem. Chem. Phys. **14**, 8299 (2012).
[20] M. Fischer, J. Handt, and R. Schmidt, Phys. Rev. A **90**, 012525 (2014).
[21] M. Fischer, J. Handt, and R. Schmidt, Phys. Rev. A **90**, 012526 (2014).
[22] M. Fischer, J. Handt, and R. Schmidt, Phys. Rev. A **90**, 012527 (2014).
[23] J. J. Bajo, G. Granucci, and M. Persico, J. Chem. Phys. **140**, 044113 (2014).
[24] H. Sambe, Phys. Rev. A **7**, 2203 (1973).
[25] S. Guerin, F. Monti, J.-M. Dupont, and H. R. Jauslin, J. Phys. A: Math. Gen. **30**, 7193 (1997).
[26] P. H. Bucksbaum, A. Zavriyev, H. G. Muller, and D. W. Schumacher, Phys. Rev. Lett. **64**, 1883 (1990).
[27] A. Giusti-Suzor and F. H. Mies, Phys. Rev. Lett. **68**, 3869 (1992).
[28] A. Giusti-Suzor, X. He, O. Atabek, and F. H. Mies, Phys. Rev. Lett. **64**, 515 (1990).
[29] J. H. Posthumus, J. Plumridge, L. J. Frasinski, K. Codling, E. J. Divall, A. J. Langley, and P. F. Taday, J. Phys. B: At. Mol. Opt. Phys. **33**, L536 (2000).
[30] M. Uhlmann, T. Kunert, and R. Schmidt, Phys. Rev. A **72**, 045402 (2005).
[31] L. J. Frasinski, J. Plumridge, J. H. Posthumus, K. Codling, P. F. Taday, E. J. Divall, and A. J. Langley, Phys. Rev. Lett. **86**, 2541 (2001).
[32] A. Fischer, M. Gärttner, P. Cörlin, A. Sperl, M. Schönwald, T. Mizuno, G. Sansone, A. Senftleben, J. Ullrich, B. Feuerstein, T. Pfeifer, and R. Moshammer, Phys. Rev. A **93**, 012507 (2016).
[33] M. Barbatti, Wiley Interdisciplinary Reviews: Computational Molecular Science **1**, 620 (2011).
[34] A. Giusti-Suzor, F. H. Mies, L. DiMauro, E. Charron, and B. Yang, J. Phys. B: At. Mol. Opt. Phys. **21**, 309 (1995).
[35] J. H. Posthumus, Rep. Prog. Phys. **67**, 623 (2004).
[36] T. Fiedlschuster, Master's thesis, Technische Universität Dresden, Dresden, 2014, http://nbn-resolving.de/urn:nbn:de:bsz:14-qucosa-157615.
[37] M. Uhlmann, T. Kunert, F. Grossmann, and R. Schmidt, Phys. Rev. A **67**, 013413 (2003).
[38] F. Bornemann, P. Nettesheim, and C. Schütte, J. Chem. Phys. **105**, 1074 (1996).

[39] U. Peskin and N. Moiseyev, J. Chem. Phys. **99**, 4590 (1993).
[40] K. Hanasaki and K. Takatsuka, Phys. Rev. A **88**, 053426 (2013).
[41] M. V. Korolkov and B. Schmidt, Comput. Phys. Commun. **161**, 1 (2004).
[42] B. D. Esry and H. R. Sadeghpour, Phys. Rev. A **60**, 3604 (1999).
[43] D. Villarejo, J. Chem. Phys. **49**, 2523 (1968).
[44] A. Abedi, N. T. Maitra, and E. K. U. Gross, Phys. Rev. Lett. **105**, 123002 (2010).
[45] S. K. Min, F. Agostini, and E. K. U. Gross, Phys. Rev. Lett. **115**, 073001 (2015).
[46] T. Fiedlschuster *et al.* (unpublished).
[47] M. Uhlmann, T. Kunert, and R. Schmidt, J. Phys. B **39**, 2989 (2006).
[48] P. N. Brown, G. D. Byrne, and A. C. Hindmarsh, [netlib.sandia.gov/ode/zvode.f].
[49] A. M. Sayler, P. Q. Wang, K. D. Carnes, and I. Ben-Itzhak, J. Phys. B: At. Mol. Opt. Phys. **40**, 4367 (2007).